ACS Photonics

pubs.acs.org/journal/apchd5

Article

# Effect of Ag Nanocube Optomechanical Modes on Plasmonic Surface Lattice Resonances

Mindaugas Juodėnas,* Domantas Peckus, Tomas Tamulevičius, Yusuke Yamauchi, Sigitas Tamulevičius, and Joel Henzie*

Cite This: *ACS Photonics* 2020, 7, 3130−3140

Read Online

ACCESS | Metrics & More | Article Recommendations | Supporting Information

**ABSTRACT:** Noble metal nanoparticles patterned in ordered arrays can interact and generate hybrid plasmonic−photonic resonances called surface lattice resonances (SLRs). Dispersion curves help explain how the Bragg coupling conditions and radiation patterns create dipolar and quadrupolar SLRs, but they assume that the nanoparticles are static structures, which is inaccurate at ultrafast time scales. In this article, we examine how local surface plasmon resonances (LSPRs) supported by cubic Ag nanocrystals are modulated by ultrafast photophysical processes that generate optomechanical modes. We use transient absorbance spectroscopy measurements to demonstrate how the LSPRs of the nanoparticles modulate the SLR of the array over time. Two primary mechanical breathing modes of Ag nanocubes were identified in the data and input into electromagnetic models to examine how fluctuations in shape affect the dispersion diagram. Our observations demonstrate the impact of optomechanical processes on the photonic length scale, which should be considered in the design of SLR-based devices.

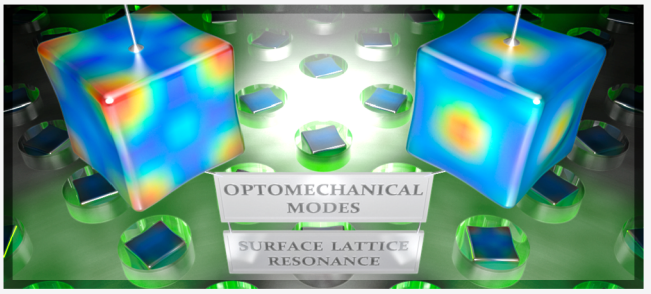


**KEYWORDS:** *plasmonics, optomechanics, photoacoustics, self-assembly, surface lattice resonances, lattice plasmons*



Decades ago theorists predicted that arrays of plasmonic nanostructures could interact collectively and generate hybrid plasmonic−photonic resonances far narrower than is possible with single nanoparticles.[1−4] In these systems, the local surface plasmon resonances (LSPRs)[5] of each particle couple with their neighbors via in-plane diffracted waves called Rayleigh anomalies (RAs). The resulting spectral peaks have quality factors (*Q*-factors, $Q = \lambda/\Delta\lambda$) an order of magnitude larger than single particles. Over time, experimentalists developed nanofabrication and optical measurement tools to observe and study these plasmonic−photonic modes.[6−12] This phenomenon is now commonly called a plasmonic surface lattice resonance (SLR) or a lattice plasmon.[6,13,14] Researchers can now engineer surfaces supporting SLRs with wide tunability and narrow spectral line width for use in novel light-emitting and light-manipulating devices.[15−19]

Transient absorption spectroscopy (TAS) has enabled researchers to better understand the dynamics of individual or isolated metal nanoparticles following the absorption of photons.[20−25] The ensuing cascade of photophysical processes underpins many of the applications of plasmonic nanostructures, but very little is known about the dynamics of highly ordered plasmonic arrays and how the ultrafast optical response of its nanoparticle constituents affect the hybrid long-range plasmonic−photonic modes of the array. At the individual nanoparticle level, the absorbed energy is transferred from the plasmon to electronic transitions and then to phonons; these phonons raise the lattice temperature and expand the lattice coordinate. Coherent optomechanical modes in metal nanoparticles can be excited when the laser pump pulse is shorter than the vibrational mode period of the particle. Ag nanoparticles with diameters >10 nm have vibrational modes at picosecond time scales.[26] The resulting ultrafast change in shape, electron density, and deformation potential modulates the intensity and wavelength of the nanoparticle LSPR at gigahertz frequencies.[25,27]

Figure 1 illustrates the length scales of the LSPR and SLR modes (*x*-axis), in addition to the time scales (*y*-axis) of their decay processes, following the absorption of a photon and generation of optomechanical modes. The optomechanical modes of individual Ag nanocubes have been studied in detail.[20,21,25,28] In brief, after a nanocube absorbs a photon, it expands and then evolves into a sum of its breathing eigenmodes. Ag nanocubes have two dominant breathing modes associated with its tips and faces.[25,27] The tip and face

**Received:** July 28, 2020
**Published:** October 20, 2020

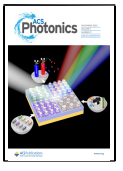

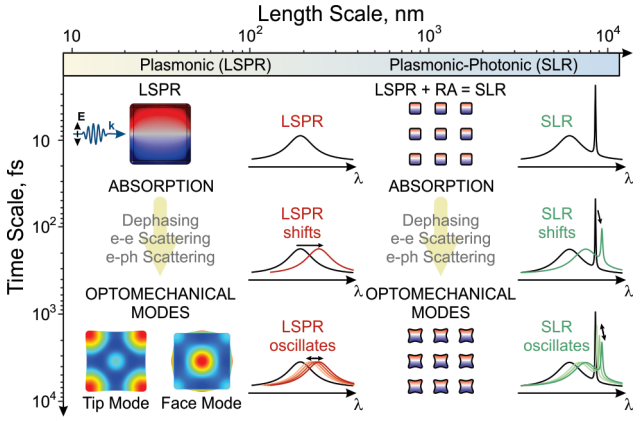


**Figure 1.** Overview of the relevant length scales and time scales described in this article. The illustration describes the processes following the excitation of individual nanoparticles (left) and nanoparticles in arrays (right) as the absorbed energy decays into optomechanical modes over time. The spectra show how a typical LSPR or SLR changes in the TAS spectrum.

modes have different frequencies and modulate the LSPR over time.[25] In the absorption spectrum of a typical dipole LSPR ("D-LSPR") (Figure 1, left), these processes cause the LSPR to shift and then oscillate as the breathing modes dissipate energy into the environment. Nanoparticles can also generate quadrupolar LSPRs ("Q-LSPRs"), which have longer dephasing times,[29] but should dissipate energy via the same process. Overall, TAS studies have demonstrated that plasmonic nanoparticles are not the static structures that appear in most computational electromagnetic models; they have a dynamic shape that affects the LSPR.[27]

Individual nanoparticles patterned into arrays with spacings on the order of the wavelength of light can couple with each other via RAs to form ultranarrow SLRs (Figure 1, right). SLRs can be composed of dipoles ("D-SLRs") or quadrupoles ("Q-SLRs") depending on the spectral overlap of the LSPR mode with RAs supported by the array. A SLR is strongly dependent on nanoparticle size/shape and its corresponding LSPR,[30] thus, we hypothesized that the optomechanical modes would also affect the time-dependent plasmonic−photonic properties. This phenomenon would be observed as an oscillation in the SLR at picosecond time scales. Other researchers have noted that the propagation of optomechanical modes on textured metal films is affected by lattice spacing,[31] and researchers in the field of Si-based optomechanical photonic crystals[32] have experimented with structures that support photonic/plasmonic bandgaps.[33] But the latter studies rely on high refractive index ($n$) dielectrics as opposed to a system that is mainly plasmonic and enables strong light−matter interactions at visible wavelengths.

In this article, we examine how dynamics on the ultrafast time scale affect optical properties that manifest on the photonic length scale. We initially compare the steady-state optical properties of free-standing, disordered colloidal Ag nanocubes suspended in solution versus the same Ag nanocubes assembled into 2D arrays that are designed to generate SLRs. The dispersion diagrams of nanoparticle arrays with various spacings were measured in an angle-dependent optical spectroscopy setup and compared to electromagnetic (EM) models generated with the finite element method (FEM). Both D-SLRs and Q-SLRs emerged from our experimental and computational dispersion diagrams. Ultrafast TAS spectroscopy was then used to measure the arrays excited at normal incidence and at 30° incidence with polarized light to examine how the in-plane versus out-of-plane SLRs evolve as the optomechanical modes ring down over time. The frequencies of the optomechanical modes were similar in colloidal solution versus in arrays because of a similar acoustic impedance of the environments. A FEM model was used to identify the dominant breathing eigenmode shapes by their frequencies: a tip mode at 27 GHz and face mode at 38 GHz. These dynamic nanoparticle shapes were then imported into the EM model to examine how the subtle change in shape modulated the dispersion diagram and affected the SLRs of the nanocube array.

## RESULTS AND DISCUSSION

**Self-Assembly of Ag Nanocube Arrays.** Researchers have used a variety of methods to generate arrays of single nanocrystals.[34−36] We used the capillary-force assisted particle assembly (CAPA)[37] technique, with PDMS patterns consisting of a square array of pits with 300, 350, and 400 nm spacings (center-to-center). PDMS templates were not preconditioned prior to assembly experiments. The assembled nanocubes have no adhesion layer and are sitting directly in circular pits patterned on a PDMS surface. The patterns were filled with monodisperse Ag nanocubes (edge length $a$ = 77 nm ±3 nm), which were generated using a variation of the polyol method.[38] Details of the CAPA method, fabrication of PDMS patterns, and synthesis of Ag nanocubes are described in more detail in Methods. The nanocubes are coated with a thin surfactant layer of 55000 molecular weight (MW) polyvinylpyrrolidone (PVP). CAPA experiments were performed using a dense solution of colloidal Ag nanocubes ($3.59 \times 10^{11}$ p/mL) in dimethylformamide (DMF) because it is a good solvent for the PVP polymer and prevents irreversible interactions between Ag nanoparticles, enabling them to behave like hard particles.[39,40] DMF also has nearly identical $n$ value as PDMS at visible wavelengths. Steady-state and TAS optical measurements on the colloidal Ag nanocube solutions were also performed in DMF ($0.28 \times 10^{11}$ p/mL). Particle concentrations were estimated using inductively coupled plasma atomic emission spectroscopy (ICP-AES). Further information can be found in previous papers[41,42] and in Methods.

Figure 2A shows a real photograph of CAPA assembly in progress on a 15 × 15 $mm^2$ array. Dark-field optical micrographs of these assemblies are shown in Figure 2B. A SEM image is shown in the close-up in Figure 2C. These images indicate a high assembly yield, which we estimate to be >99% in a >1 $cm^2$ area (estimated from a randomly selected 40 × 40 $\mu m^2$ area with $n$ = 10000 events). The assembled nanoparticle patterns could be left exposed to air to generate an asymmetric dielectric environment or fully encapsulated by polymerizing an additional layer of PDMS following deposition to create a uniform dielectric environment. We mainly focused on the asymmetric patterns with nanoparticles exposed to the environment because this configuration may be advantageous for sensing applications as it leaves the superstrate open for the introduction of different analytes.

**UV−Vis Measurements of Colloidal Ag Nanocubes in Solution versus Ordered Arrays.** Figure 3A shows the absorbance spectrum of a solution of colloidal Ag nanocubes ($a$ = 77 nm) suspended in DMF. Free-standing Ag nanocubes support numerous bright and dark plasmon modes.[43−45] We


https://dx.doi.org/10.1021/acsphotonics.0c01187
ACS Photonics 2020, 7, 3130−3140

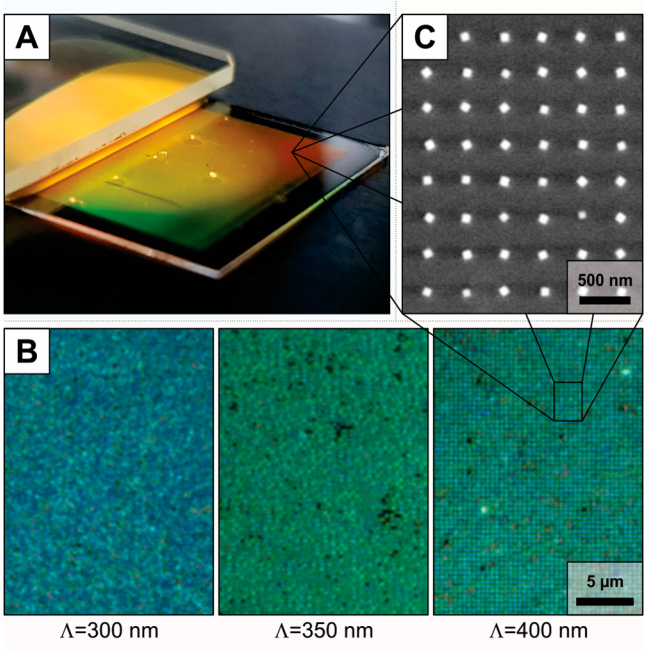


**Figure 2.** Nanoparticle self-assembly. (A) Photograph of the CAPA assembly process drawing a nanoparticle ink across a 15 × 15 $mm^2$ template. (B) Dark-field optical micrographs (100×, NA = 0.9) of nanocube arrays with 300, 350, and 400 nm spacings. (C) SEM micrograph of a self-assembled nanocube lattice.

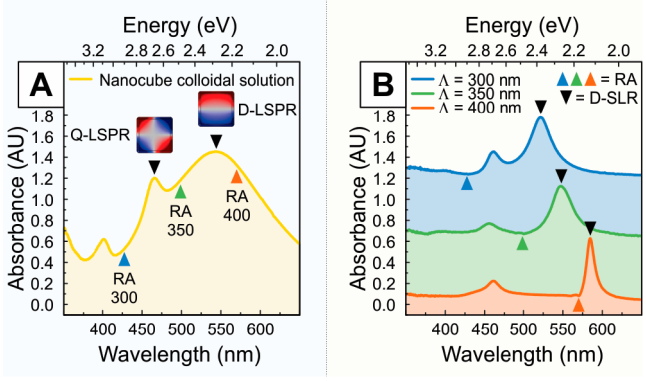


**Figure 3.** Optical properties of nanocubes in solution vs in arrays. (A) Steady-state UV−vis spectrum of a colloidal solution of Ag nanocubes ($a$ = 77 nm). The location of the D-LSPR and Q-LSPR peaks and RAs are labeled on the spectrum. (B) Steady-state UV−vis spectrum of nanocube arrays with spacings of 300, 350, and 400 nm excited at normal incidence. The spectra are offset for clarity. The SLRs and RA wavelengths at normal incidence (Γ points) of each lattice spacing are marked with triangles.

calculated the charge distribution plots of the D-LSPR and Q-LSPR of the nanocubes and labeled their location in Figure 3A. The RAs are also labeled in the graph to show where they would overlap with the LSPRs. Arrays containing the same cubes were assembled, and their transmission properties were measured at normal incidence with a collimated incandescent light source and a 6 mm diameter lens fiber coupled to a spectrometer (Figure 3B). The RA wavelengths at normal incidence for square gratings in PDMS are $\lambda_{RA} = \Lambda \times n$. Thus, for Λ = 300, 350, and 400 nm square gratings in PDMS ($n$ = 1.425), $\lambda_{RA}$ is 428, 499, and 570 nm (marked with colored triangles). Their corresponding SLRs are located at wavelengths of 522, 549, and 585 nm (marked with black triangles in Figure 3B). The wavelengths are expressed in both nanometers and electron volts (eV) to help the reader identify these resonances in the dispersion diagrams later in this article.

The relative spectral position between the RA and LSPR resonance is the most critical factor for SLR coupling.[3,4,8] Of all the arrays described here, only the 400 nm lattice RA is on the red side of the single nanoparticle D-LSPR at normal incidence, giving a narrow dipolar SLR (D-SLR) peak ($Q = \lambda/\Delta\lambda \approx 48$). The other two arrays have similar line widths ($Q \approx 18$ and $Q \approx 14$ for 350 and 300 nm lattices, respectively) at different spectral positions, which is associated with the relative positions of their respective RAs. Neither of the normal incidence RAs match the wavelength of the narrow Q-LSPR peak at ∼460 nm. Therefore, the quadrupolar SLR (Q-SLR) can only be observed with off-normal excitation because it affects the spectral position of the RA according to the energy dispersion relation: $E = \frac{\hbar c}{n}\left|\vec{G} + \vec{k}_{||}\right|$, where $n$ is the refractive index of the medium, $\vec{G}$ is the reciprocal lattice vector, and $\vec{k}_{||}$ is the in-plane projection of the wavevector. The PDMS- and air-propagating RAs are shown in Figure 4A.

**Dispersion Diagrams of Nanocube Arrays and the Relevance of Single-Nanocube Radiation Patterns.** The energy dispersion diagrams for each array were collected from 0−90° incidence with TM and TE polarization in transmission mode (Figure 4B−D). The calculated RA lines are overlaid on top. In between each dispersion diagram is a greyscale bar representing the UV−vis absorption spectrum of the free-standing Ag nanocubes suspended in solution for reference in order to compare the location of the LSPRs with the SLRs. To eliminate redundancy and allow a better comparison between the three cases, we only plot the first Brillouin zone of the square unit cell (i.e., the in-plane $k$-vector range $-\pi/\Lambda$ to $\pi/\Lambda$). These results clearly show the dependence of coupling on the in-plane polarization of the nanoparticle arrays, which we previously described using a hexagonal lattice of Ag nanoparticles.[42] When the nanocube is excited with TM-polarized light, its radiation pattern couples most strongly to the (0, ±1) modes. TE-polarized nanoparticles couple most strongly to the (±1, 0) modes. This is easily observed in the dispersion diagram of the Λ = 400 nm (Figure 4B) lattice because its RA is on the red side of the nanocube D-LSPR; hence, the peak is very narrow. The TM case shows a parabolic SLR following the (0, ±1) modes, whereas the TE case has a strongly red-shifting SLR peak following the (±1, 0) modes. This coupling preference persists in all nanoparticle array samples examined in this article.

When the arrays are excited with TM-polarized light at larger angles of incidence, the electric field vector becomes increasingly polarized perpendicular to the plane of the array. These conditions enable out-of-plane SLRs that have been observed by us[42] and other research groups.[12,46−50] In out-of-plane excitation, the radiation pattern of a dipole lies in the array plane, enabling coupling to any of the modes. It manifests in the experiment as coupling to unexpected directions, such as coupling to (±1, 0) modes using TM polarization. Out-of-plane resonances are challenging to observe experimentally because the nanoparticle patterns are typically designed to achieve the narrowest SLR peaks at normal incidence; the RA is usually designated further to the red-side of particle LSPR, but the RA shifts quickly as the angle of incidence is changed,


https://dx.doi.org/10.1021/acsphotonics.0c01187
ACS Photonics 2020, 7, 3130−3140

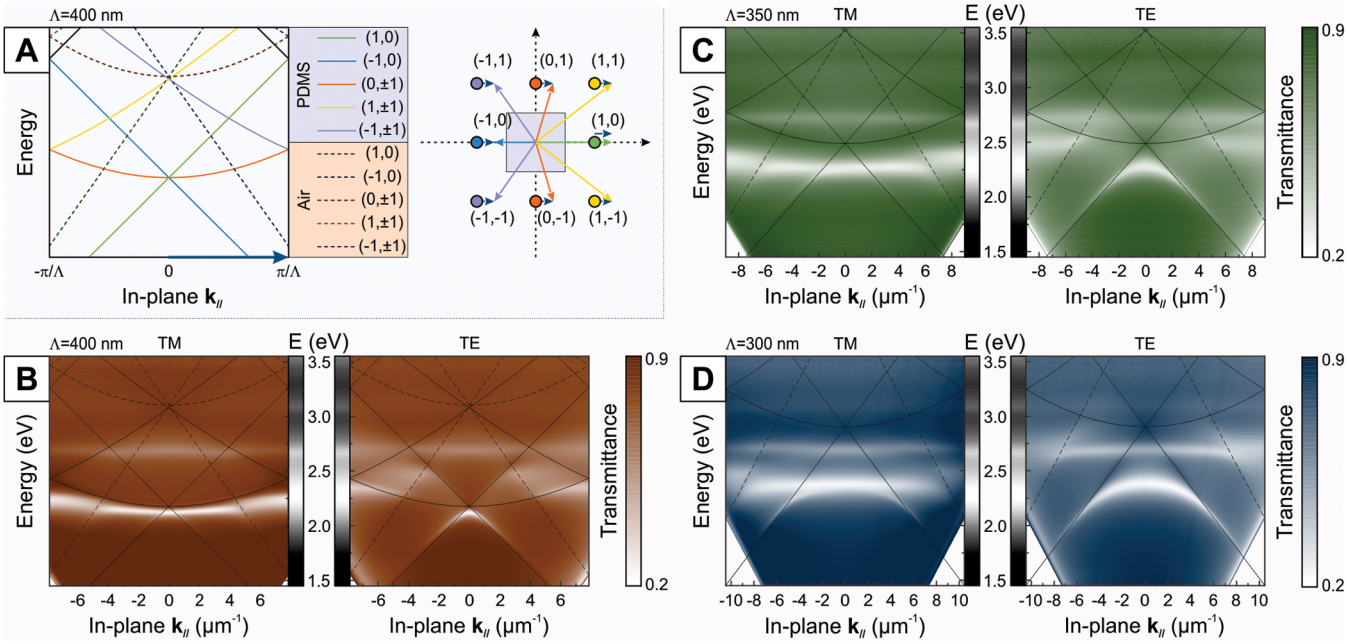


**Figure 4.** Energy dispersion diagrams of the self-assembled nanocube arrays. (A) Energy dispersion structure of a square lattice; diffraction orders propagating in two interfacing media are plotted: PDMS $n$ = 1.425 and air $n$ = 1. A reciprocal lattice diagram shows the modification of lattice vectors because of additional in-plane light momentum provided by off-normal excitation; (B–D) Steady-state $E-k$ dispersion diagrams of nanocube arrays with 400 (B), 350 (C), and 300 nm (D) spacings. The $E-k$ diagrams were collected in transmission mode using a collimated white light that is TM- or TE-polarized. The calculated RA lines are overlaid on top. The vertical greyscale bars represent the transmission spectrum of colloidal Ag nanocubes in solution (see Figure 3A).

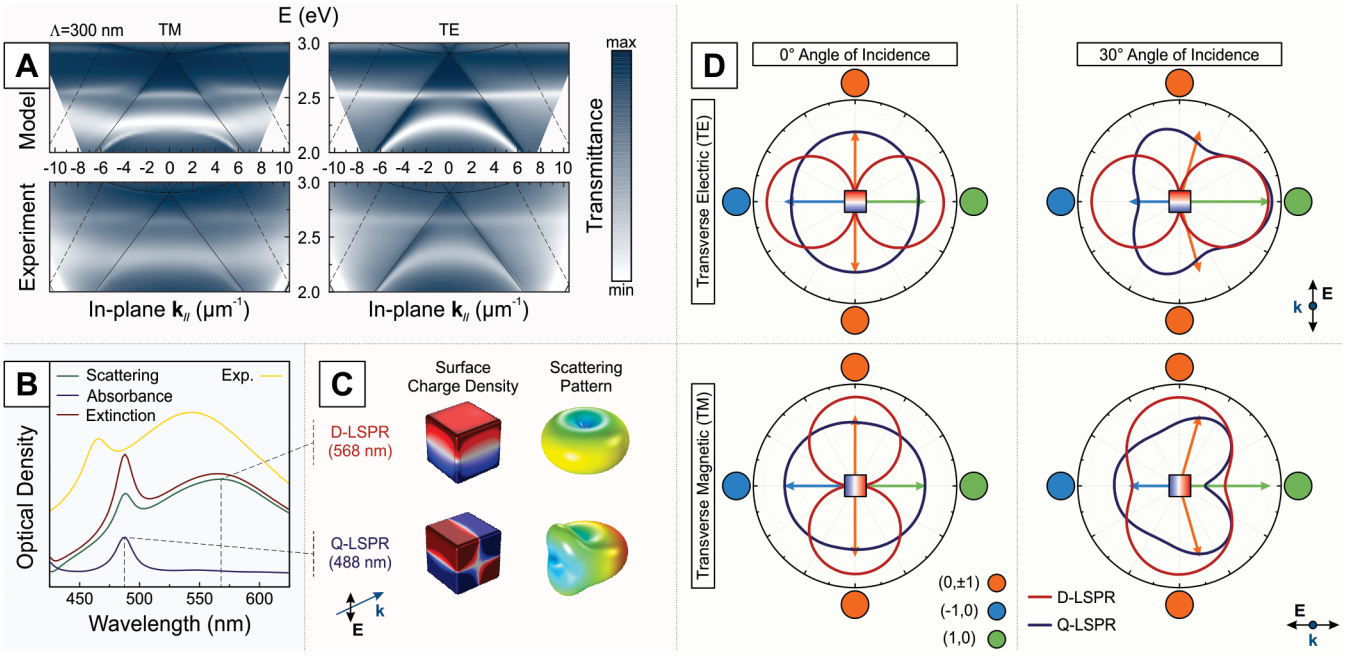


**Figure 5.** FEM modeled nanocubes and their arrays. (A) Simulated (top) and experimental (bottom) energy dispersion diagrams of a 300 nm spaced nanocube lattice in a homogeneous slab of PDMS. Transmittance is normalized (actual value ranges are 0.015–0.98 in the model and 0.15–0.625 in the experiment). (B) Experimental and simulated absorption spectra of the nanocube colloid solution. (C) Respective surface charge density and radiation pattern surfaces. (D) Polar plots of in-plane radiation patterns generated by the Q-LSPR and D-LSPR modes at normal incidence and at 30° incidence.

and large angles required to polarize nanoparticles out-of-plane causes the RA to red-shift too far away from the single-particle LSPR. Thus, coupling is weak, but the SLR retains its narrow line width. This phenomenon is evident in the TM polarized excitation of the Λ = 400 nm (Figure 4B) and 350 nm spaced arrays (Figure 4C). There are sharp features following the (±1, 0) PDMS-propagating modes (marked as solid green and blue lines in Figure 4A). However, they quickly fade because the RA red-shifts too far away from the single-particle LSPR. Strong out-of-plane coupling extends further in the 300 nm (Figure


https://dx.doi.org/10.1021/acsphotonics.0c01187
ACS Photonics 2020, 7, 3130–3140

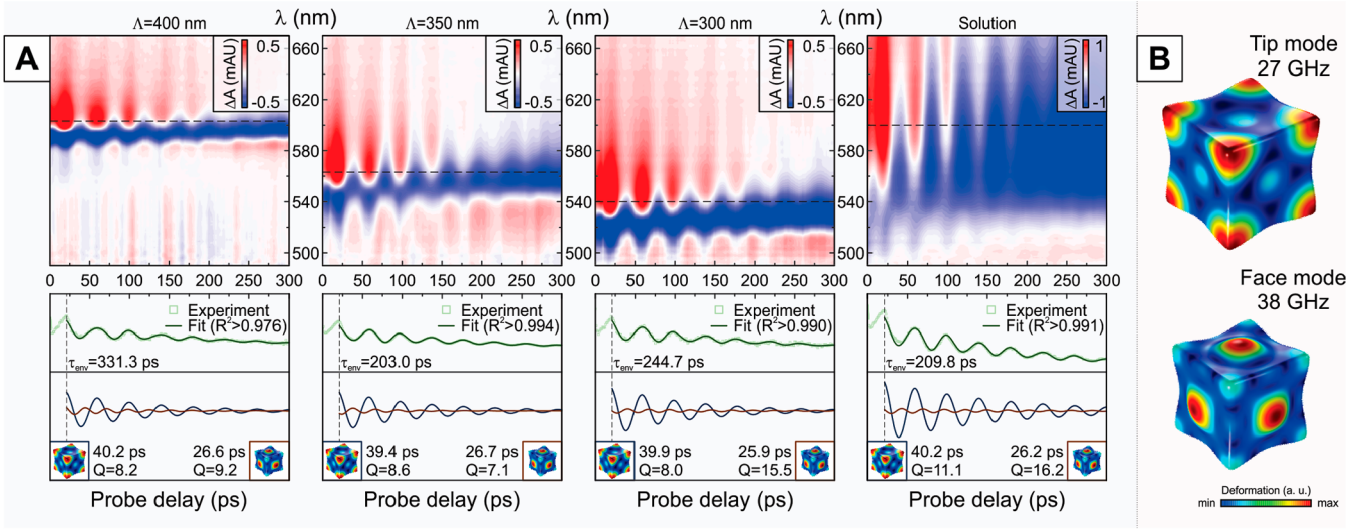


**Figure 6.** Transient absorption measurements of arrays exhibit the signature of fundamental optomechanical modes of single nanocubes. (A) Transient absorption spectroscopy carpets were collected on arrays with spacings Λ = 400, 350, and 300 nm at normal probe incidence and compared to a colloidal solution containing the same nanocubes. The horizontal dashed lines indicate the traces used to fit the optomechanical modes ($\lambda_{probe}$ = 603, 563, 540, and 601 nm for each respective case, left to right). The traces were fit using a sum of a decaying exponent and two damped cosines starting from $t$ = 21 ps to eliminate the uncertainties introduced by a mixed contribution to the TAS signal from e-ph equilibration and crystal lattice expansion. (B) The two dominant eigenshapes were modeled with FEM: tip mode (27 GHz) and face mode (38 GHz).

4D) spaced lattice ($Q \approx 78$ at $\theta = 35°$) because the RAs still intersect the single-particle LSPR at oblique angles of incidence, allowing the nanoparticles to be polarized normal to the surface. These types of SLRs are particularly interesting because their EM field is concentrated out-of-plane instead of in-plane, which may enable extreme sensitivity to changes in the dielectric environment.

The Q-LSPR peak, observed in all dispersion diagrams at ~2.65 eV, remained relatively constant and independent of array spacing. The colloidal solution spectrum in Figure 3A shows that the Q-LSPR and D-LSPR should be similar in intensity, whereas the latter is invisible in the arrays. The number of particles probed in solution ($5.42 \times 10^8$ nanoparticles) versus in the arrays ($1.23 \times 10^8$, $1.6 \times 10^8$, and $2.18 \times 10^8$ nanoparticles for 400, 350, and 300 nm patterns, respectively) is on the same order of magnitude. So we attribute this feature to the combined effects of phase retardation and substrate-induced quadrupole-dipole hybridization.[44,51]

The Q-SLR could be observed at larger angles and appears in TE illumination in the 300 nm spaced arrays (Figure 4D). Interestingly, it is formed next to the air-RA $(\pm1, 0)$ at $k \approx 8$ $\mu m^{-1}$ instead of the PDMS-RA $(\pm1, 0)$ at $k \approx 2$ $\mu m^{-1}$ (marked with solid and dashed lines in Figure 4A, respectively). This behavior can be explained by extending the plasmon hybridization theory for single nanocubes on surfaces to SLRs.[44] The nanocube array is partially exposed to air, so there are two RAs available in this asymmetric dielectric environment—one propagating above the array in air, and one propagating in PDMS below. The D-LSPR EM intensity is expected to be localized in the larger $n$ medium and thus interacts strongly with the PDMS-RA. The dispersion diagrams in Figure 4 illustrate this point because the strong dipolar SLR peaks are close to the PDMS-RAs. In contrast, substrate-induced hybridization causes the Q-LSPR mode to shift primarily into the air superstrate[44] and interact with the air-RA.

We performed EM modeling using FEM with a single nanocube, and nanocubes in Λ = 300 nm spaced square arrays. The arrays were suspended in a homogeneous dielectric environment ($n$ = 1.43) to simplify the calculations. To make a direct comparison, we also prepared a nanocube array sample fully encapsulated in PDMS (Figure 5A). The modeled $E-k$ dispersion maps match the experiment almost perfectly. However, there is a slight red-shift in the modeled peaks due to the unavoidable mismatch between nanoscale features and bulk-derived optical constants. The red-shift is also observed in the single-nanocube model (Figure 5B). As expected, the features previously attributed to air-RAs have disappeared in uniform $n$, and the D-SLRs remain mostly unchanged compared to air-exposed samples in Figure 4D because the PDMS-RAs dominate the D-SLRs in both cases.

Interestingly, the Q-SLR coupling has shifted from TE to TM polarization in both the simulation and experiment. We use the radiation patterns of the D-LSPR and Q-LSPR modes to help explain this observation. The radiation pattern of the nanocube D-LSPR mode has a characteristic torus shape that allows it to best couple to RAs that match the radiation direction (Figure 5C,D). As a result of the symmetry of the D-LSPR in TE excitation, coupling preference does not change with the angle of incidence. In the TM case, the toroidal radiation pattern progressively rotates with the angle of incidence, allowing out-of-plane coupling described earlier. Figure 5D shows cross sections of the radiation patterns when the angle of incidence is normal (left) and 30° (right). The radiation pattern of the nanocube in the lattice will be different due to fields generated by neighboring particles, but the coupling rules are similar. The radiation pattern of the Q-LSPR is different; it has a fishtail-like shape in the backscattering direction, which shifts the radiation pattern node away from the center of the particle. Thus, the radiation pattern cross-section in the plane of the array is an ellipse at normal incidence, which means that the quadrupole radiates in-plane in all directions, enabling it to couple to any RA. But the


https://dx.doi.org/10.1021/acsphotonics.0c01187
ACS Photonics 2020, 7, 3130−3140

quadrupolar peak is very narrow and thus extremely sensitive to lattice spacing. Predicting the correct lattice spacing with imperfect optical constants is challenging; thus, we did not observe Q-SLR at normal incidence in the arrays tested, but it should be possible. Figure 5D also shows the profile of the Q-LSPR radiation pattern at a 30° angle. In TE excitation, scattering is strongest in the (1, 0) direction. However, this direction corresponds to an RA with energy that increases with the angle of incidence, and the quadrupole is already smaller in energy than the RA, so coupling is not possible in TE excitation. In TM excitation, there is stronger radiation in the (−1, 0) direction, which corresponds to an RA with decreasing energy, allowing it to intersect with the quadrupolar LSPR and couple into the Q-SLR at high angles of incidence. The reason for the switch of the Q-SLR from TE to TM is not completely clear; we speculate that the radiation pattern of Q-LSPR in an asymmetric environment might be modified in a way that reverses the coupling priority observed in a homogeneous environment.

**TAS Measurements of Colloidal Ag Nanocubes in Solution versus in Ordered Arrays.** Figure 6A shows TAS plots with $\Delta A$ modulations that are characteristic of optomechanical modes supported by plasmonic nanoparticles. We measured all array samples ($\Lambda$ = 400, 350, and 300 nm) in addition to colloidal Ag nanocubes suspended in DMF (i.e., "Solution"). There have been efforts to examine the collective mechanical modes of small clusters of Au nanoparticles,[52] nanowire arrays composed of indium tin oxide (ITO),[53] and various nanoparticle arrays.[54,55] In particular, the experiments on Au clusters show that near-field coupling can enable the hybridization of vibrational modes of closely spaced nanoparticles.[52] The work on ITO nanowires shows how vibrational modes can modulate transmittance over time. To our knowledge, there are no previous experiments explaining how optomechanical modes affect plasmonic SLRs at ultrafast frequencies.

Cubes are known to support two vibrational breathing modes that dominate its mechanical response.[25,27] The strongest mode results from a deformation of the eight corners of the cube. We call this the "Tip Mode" and it is known to strongly affect the position and intensity of the LSPR. The second mode is a higher-frequency overtone resulting from the deformation of the six faces of the cube. We call this the "Face Mode" and note that it has a smaller effect on the LSPR. An eigenmode analysis was performed on a single Ag nanocube suspended in a vacuum with FEM. A menagerie of these eigenmodes is shown in Supporting Information, Figure S1. The two most dominant breathing modes were selected based on fitting results and plotted in Figure 6B. To understand the impact of each vibrational mode on TAS data, we selected TAS traces with the highest signal amplitude and plotted in the bottom row of Figure 6A. Each trace was analyzed using a machine learning (ML) algorithm (Eureqa) by fitting it with a decaying exponential ($e^{-t/\tau_{env}}$; $\tau_{env}$ is the decay constant) and two damped cosine functions.[25] The fit was initiated at $t$ = 21 ps to minimize the contribution of e-ph equilibration and focus on lattice expansion/contraction. In the ML code, the face mode was constrained to be smaller in amplitude than the tip mode. In addition, frequencies were selected to best match those acquired after performing a fast Fourier transform (FFT) on the data (Supporting Information, Figure S2). The ML code was allowed to run until it achieved a high goodness-of-fit ($R^2$ > 0.97). The optomechanical mode-defining parameters are given in Supporting Information, Table S1. The mechanical quality factors for each mode is expressed as $Q = \frac{\pi\tau}{T}$, where $\tau$ and $T$ are the decay constant and the period of the damped cosine function in $e^{-t/\tau}\cdot\cos\left(\frac{2\pi t}{T} - \varphi\right)$. These equations are used to compare how each array affects the damping of optomechanical modes.

The mechanical $Q$-factors of nanoparticles depend on their materials and dimensions, in addition to the acoustic impedances of the surrounding media.[56] Previously, Hartland et al. measured individual Ag nanocubes cast with poly(vinyl alcohol) on glass substrates and observed $Q$-factors from 14 to 25.[28] Damping of the $Q$-factor of metal nanostructures is highly dependent on the orientation of the particle and its interaction with a solid substrate. Since our nanoparticles are randomly oriented in the circular pits and exposed to the air-PDMS interface, we expect larger inhomogeneous broadening that will lead to some decrease in $Q$-factor.

In the colloidal solution, the D-LSPR of the nanocubes is very broad due to the intrinsic radiative damping of bright plasmon modes. The $Q$-factors of the tip and face modes were 11.1 and 16.2, respectively, at $\lambda_{probe}$ = 601 nm. Interestingly, the $Q$-factor should be larger in ethanol,[21] because ethanol has a smaller acoustic impedance (0.9 MPa·s/m) than DMF (1.37 MPa·s/m). But DMF is a much better solvent for PVP polymer (1.2 MPa·s/m). Swelling the PVP surfactant with DMF may lead to a smaller average acoustic impedance resulting in the larger observed $Q$-factor. The $Q$-factors of the optomechanical modes in arrays excited at normal incidence (0°) are smaller than the colloidal solution measurements ($Q \approx 8$ for the tip mode and $Q \approx 7-15$ for face mode). A few points are worth noting are as follows: (i) The tip mode has a near-constant $Q$-factor in all array samples; (ii) The face mode varies between samples and becomes strongest in the $\Lambda$ = 300 nm pattern.

**Influence of Optomechanical Modes on SLRs.** The SLR depends on the RA and LSPR in a nanoparticle array. The position of the RA is fixed in our experiment. Thus, any change in the LSPR will affect coupling to the RA and modify the SLR peak. The effect of chemically deforming Ag nanocubes on the LSPR has been studied by colloidal chemists and serves here as a useful guide.[57] They show that the LSPR progressively red-shifts as the faces become concave and tips extend away from the body center of the cube. Conversely, Ag nanocubes with rounded edges and tips have blue-shifted LSPRs. To understand how dynamic mechanical deformation of the nanocube affects the SLR, we used TAS to measure the $\Lambda$ = 300 nm array using a pump/probe incidence angle of 30° with TE and TM excitation (Figure 7). At 30° incidence, TM polarization produces two peaks, one in-plane and one out-of-plane; we will consider the former and compare it to TE-generated in-plane coupling. The EM intensity plots in Figure 7 demonstrate the characteristic in-plane and out-of-plane intensity distribution, and the out-of-plane mode generates stronger fields. Regarding optomechanical modes, the tip mode maintained the same $Q$-factor in both in-plane and out-of-plane coupling and matched previous experiments at 0° incidence ($Q \approx 9$). Interestingly, the face mode $Q$-factor was larger in the in-plane case ($Q \approx 12$). The larger $Q$ in-plane could be a consequence of increased elastic environment homogeneity in the plane of the array versus out of plane, because the latter has one facet strongly adsorbed to the polymer surface.


https://dx.doi.org/10.1021/acsphotonics.0c01187
ACS Photonics 2020, 7, 3130−3140

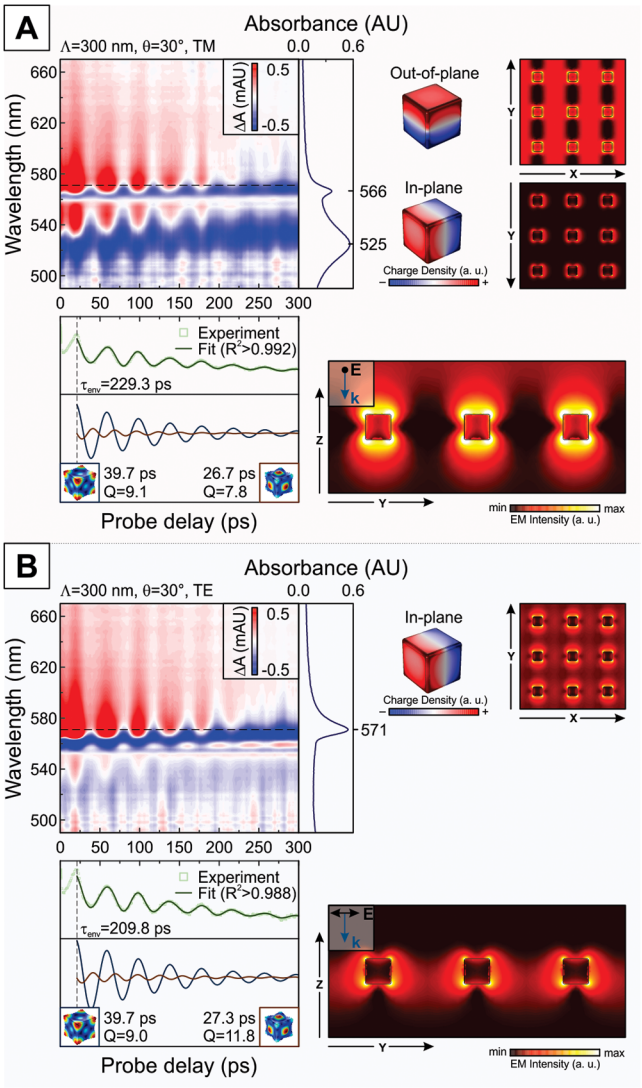


**Figure 7.** Transient absorption measurements at an angle. Transient absorption data taken from 300 nm spaced nanocube arrays at 30° probe angle of incidence and two polarizations: (A) TM and (B) TE. Traces used for fitting are marked with a horizontal dashed line ($\lambda_{probe}$ = 571 nm). The absorption spectra next to the 2D maps are steady-state measurements taken at the same angle of incidence. Surface charge density maps of the nanocubes are presented next to the respective absorption peaks, and the electric field time average is plotted in the *XY* and *YZ* planes of the nanoparticle array.

A finite element study in the frequency domain was performed on a Λ = 300 nm square array with the tip and face mode eigenshapes to study how the SLR was affected by them over time. Initially, we performed a frequency sweep of a nanocube (a displacement relation of characteristic points on a nanocube can be found in Supporting Information, Figure S3). As predicted by the eigenmode analysis, the edge mode and face mode are very close in frequency, becoming convoluted when isotropic damping is used, yielding a combined shape at the face mode frequency.[25,27] Therefore, to produce pure tip and face mode shapes, we used the frequencies of dominant eigenmodes with Rayleigh damping, which damps all but two predefined frequencies. The initial strain was selected to yield a deformation of 3 nm to observe clear shapes. A comparison to the TAS signal generated by a 1 nm maximum amplitude can be found in Supporting Information, Figure S4, which shows that the general shape of the TAS curves remains the same. We select the phase of both modes with the tips of the nanocubes extended outward (the shapes at $\pi$-shifted phases can be found in Supporting Information, Figure S5). Each array was modeled using an incident excitation from 0−30° and then subtracted from the $E-k$ diagram acquired from a lattice of Ag nanocubes with the original undistorted cubic shape (Figure 8A).

The dispersion diagrams in Figure 8A are strongly affected by the deformed shapes that represent the optomechanical modes. Both modes cause a red-shift in the spectrum. We only consider the influence of shape on LSPR, but changes in electron density and interband transitions will also play a role but to a lesser extent in cubes.[27] The tip mode dominates the overall change of the optical response, which is demonstrated by the amplitude and distance between the positive and negative $\Delta A$ peaks. The D-SLRs of both tip and face modes generate similar patterns in both TE and TM excitation, including the out-of-plane mode. The Q-SLR available in TM excitation is most strongly affected, $+\Delta A$ contributions from the tip and face mode almost do not overlap in energy. This strong contrast difference between the Q-SLRs of the tip and face modes could be caused by the Fano line shape of quadrupolar modes,[44] which is very sensitive to changes in the shape of the corners and edges of nanocubes.[58]

The simulated ΔA spectra from 0° and 30° (TM/TE) illumination schemes were compared to the Λ = 300 nm arrays in the experiments (Figure 8B). We focus on the D-SLR here because its features are well within the bandwidth of the probe in our experimental TAS setup. Under normal excitation, both arrays cause the SLR to red-shift versus the undeformed nanocube array, matching the shape and general shift in the experiment. The experimental trace also features a slightly asymmetric line shape, indicating a broadening of the SLR peak. TE and TM excitation generated slightly smaller red-shifting of the SLR in the simulated arrays. Probing at an angle and especially at the sharpest out-of-plane mode wavelength enables us to exploit the narrow line shape of the SLR, even though the shift is smaller, the amplitude of the signal is larger than normal excitation because very small changes of a sharp feature can generate strong differences in the TAS signal. Overall, the simulations have an excellent qualitative match with the experiments, even with the large deformation of the simulated eigenmodes. These results indicate that the dynamic shape of the nanoparticle may also be considered when designing SLR-employing devices for ultrafast applications such as lasers.[59] For example, SLRs could be designed with strong $\Delta A$ that modulates the intensity and position of the SLR. If the modulation generates strong enough $\Delta A$ it may enable pulsed light emission at gigahertz frequencies in an appropriate gain medium.

## CONCLUSIONS

Previous work on SLRs has focused on the fundamental interaction between LSPRs and RAs in Bragg scattering conditions. Our work shows how absorption can modify the LSPR and alter the dynamic optical properties of the SLR over time. First, we investigated steady-state optics of nanocube arrays and explained how LSPRs interact via RAs and form in-plane and out-of-plane D-SLRs and Q-SLRs. Later we compared the optomechanical properties of free-standing Ag nanocubes suspended in solution vs nanocubes in arrays under Bragg coupling conditions. The arrays generate similar


https://dx.doi.org/10.1021/acsphotonics.0c01187
ACS Photonics 2020, 7, 3130−3140

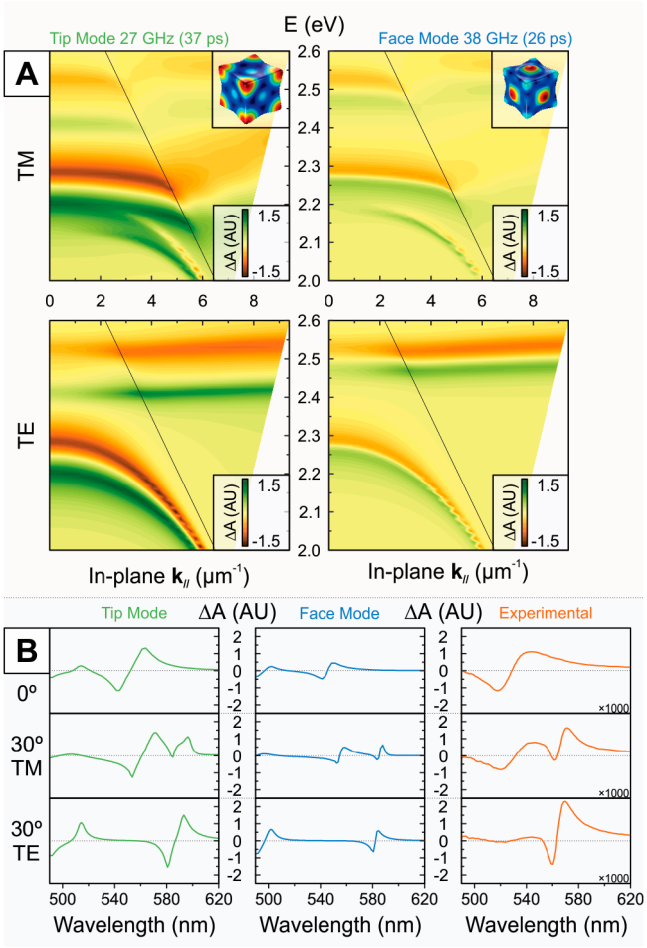


**Figure 8.** Influence of the isolated eigenmodes on the $E-k$ diagrams. (A) Absorbance difference maps on $E-k$ diagrams, showing the individual contribution of the two primary modes to the TAS signal. The calculated RA is overlaid on top; (B) Absorbance difference traces generated by tip mode (left), face mode (middle), and experimental measurement (right, multiplied by a factor of 1000 for clarity) at normal (top) and 30° incidence with TM/TE polarizations (bottom).

mechanical quality factors even though their viscoelastic environment is anisotropic. TAS measurements at high angles revealed that the in-plane mode couples more effectively to the mechanical modes compared to out-of-plane mode, but the latter has the advantage of narrower spectral line width. A full eigenmode analysis of the mechanical modes of cubes was performed to determine the shapes of the two dominant eigenmodes. These two eigenshapes were imported into our electromagnetic model to show how deformation affects the dispersion diagram of the nanocube array. The dynamic shape of the nanocube affects the SLR over time and matches our experimental TAS data showing the contribution of each optomechanical mode. This work shows how local vibrational modes can shift and modulate photonic/plasmonic modes at ultrafast time scales. This phenomenon may impact applications such as nanolasing and light collection and perhaps be used to create new functions.

## METHODS

**Nanoparticle Synthesis/Characterization.** The particles are synthesized using a variation of the Ag polyol method.[38] The average edge length ($a$) of the ensemble of cuboctahedra was measured using a JEOL-1010 TEM operating at 100 kV with a minimum magnification of <0.5 nm/pixel. A total of 200 nanoparticles were measured, and the average size was $a$ = 77 ± 3 nm. The particles were suspended in DMF at a concentration of 3.59 × $10^{11}$ p/mL, as determined by inductively coupled plasma atomic emission spectrometry. The Ag nanocubes are coated with a layer of polyvinylpyrrolidone (PVP; 55000 MW) polymer surfactant. The PVP serves as a steric barrier to minimize uncontrolled aggregation even at high nanoparticle concentrations.[39,40]

**Capillary Force Assisted Assembly (CAPA).** The master stamps (Si) featuring pillars for template preparation where fabricated using e-beam lithography, Al lift-off, and reactive ion etching using $SF_6/C_4F_8$ plasma. These stamps were coated with a self-assembled monolayer of perfluorooctlytrichlorosilane as an antiadhesion layer. Soft lithography was employed to create polymer templates by casting and thermally curing polydimethylsiloxane. The resulting patterned substrates were used in a custom capillary force assisted assembly setup.[41] During the deposition process, a temperature-controlled stage translates the vacuum chucked sample relative to a stationary microscope glass slide. A droplet of colloidal nanocubes suspended in DMF is confined between the substrate and the glass slide. The recirculation currents because of the movement and evaporation flow bring nanoparticles from the bulk of solution close to the meniscus, where nanoparticles accumulate and eventually deposit into pits defined by the master stamp. The nanoparticle assemblies are investigated using optical darkfield and scanning electron microscopy as well as a custom free-space UV−vis angular spectrophotometry setup.[60]

**Transient Absorption Measurements.** Ultrafast relaxation processes in Ag nanocubes (both in solution and regular 2-D structures) were investigated by means of transient absorption spectroscopy (TAS). HARPIA spectrometer built by Light Conversion was used for TAS measurements. The samples were excited using a Pharos ultrafast Yb:KGW laser (Light Conversion) with a regenerative amplifier at a 66.7 kHz repetition rate and 290 fs duration pulses at 1030 nm wavelength. The pump beam wavelength was tuned with a collinear optical parametric generator Orpheus and harmonic generator Lyra (Light Conversion) to 350 nm and an energy density of 40 $\mu J/cm^2$. The samples were probed with a white light supercontinuum generated using a 2 mm thickness sapphire plate excited with a fundamental laser wavelength. The spectral range of the supercontinuum probe as well as the detection range of the TAS dynamics spanned wavelengths from 489 to 793 nm. The excitation beam was focused down to a ∼700 $\mu$m diameter spot. The supercontinuum probe was ∼500 $\mu$m in diameter. The steady-state absorption of samples was rechecked after each measurement to ensure there was no damage from the laser irradiation.

**Modeling.** Finite element modeling was performed using COMSOL Multiphysics suite. The Structural Mechanics Module was employed for the mechanical response of the nanoparticle. Eigenmode analysis and the frequency response was modeled using the geometry of the synthesized nanoparticles and mechanical material properties provided by the integrated material library. Optical modeling was done using the RF Module. For single-particle modeling, a nanoparticle was placed in a uniform dielectric environment, surrounded by a perfectly matched layer, and the background field was designed as a plane wave. The far-field border layer was


https://dx.doi.org/10.1021/acsphotonics.0c01187
ACS Photonics 2020, 7, 3130−3140

designated as the surface between the physical dielectric domain and the perfectly matched layer. The optical constants of silver were implemented in the model using data collected by Johnson and Christy.[61] For array modeling, the nanoparticle was placed in a dielectric with Floquet boundary conditions relating to the square pattern. The array was illuminated from a port above the nanoparticle at varying incidence angles and polarizations, and a secondary port below collected the transmitted light, yielding transmittance spectra.

## ■ ASSOCIATED CONTENT

### Supporting Information

The Supporting Information is available free of charge at https://pubs.acs.org/doi/10.1021/acsphotonics.0c01187.

Eigenmode analysis of a Ag nanocube (Figure S1); FFT of a TAS trace (Figure S2); A table containing the fitting parameters (Table S1); Frequency domain analysis of a Ag nanocube's deformation (Figure S3); A comparison between two TAS spectra modeled with different deformation amplitudes (Figure S4); $\pi$-shifted phases of the Ag nanocube mechanical modes (Figure S5) (PDF)

## ■ AUTHOR INFORMATION


### Corresponding Authors

**Mindaugas Juodėnas** − *Institute of Materials Science, Kaunas University of Technology, Kaunas LT-51423, Lithuania;* orcid.org/0000-0002-0517-8620; Email: mindaugas.juodenas@ktu.lt

**Joel Henzie** − *International Center for Materials Nanoarchitectonics (WPI-MANA), National Institute for Materials Science (NIMS), Ibaraki 305-0044, Japan; JST-ERATO Yamauchi Materials Space-Tectonics Project, Saitama 332-0012, Japan;* orcid.org/0000-0002-9190-2645; Email: joelhenzie@protonmail.ch

### Authors

**Domantas Peckus** − *Institute of Materials Science, Kaunas University of Technology, Kaunas LT-51423, Lithuania;* orcid.org/0000-0002-4224-2521

**Tomas Tamulevičius** − *Institute of Materials Science and Department of Physics, Kaunas University of Technology, Kaunas LT-51423, Lithuania;* orcid.org/0000-0003-3879-2253

**Yusuke Yamauchi** − *Australian Institute for Bioengineering and Nanotechnology (AIBN) and School of Chemical Engineering, The University of Queensland, Brisbane, Queensland 4072, Australia; JST-ERATO Yamauchi Materials Space-Tectonics Project, Saitama 332-0012, Japan;* orcid.org/0000-0001-7854-927X

**Sigitas Tamulevičius** − *Institute of Materials Science and Department of Physics, Kaunas University of Technology, Kaunas LT-51423, Lithuania;* orcid.org/0000-0002-9965-2724

Complete contact information is available at: https://pubs.acs.org/10.1021/acsphotonics.0c01187


### Author Contributions

The manuscript was written via the contributions of all authors. All authors have given approval to the final version.

### Notes

The authors declare no competing financial interest.

## ■ ACKNOWLEDGMENTS

M.J., D.P., T.T., and S.T. acknowledge funding from the Research Council of Lithuania (LMTLT) (Agreement No. S-LLT-18-2) and the Ministry of Science and Technology of Taiwan. J.H. acknowledges the World Premier International Research Center Initiative on Materials Nanoarchitectonics (WPI-MANA) from MEXT, and the Japan Society for the Promotion of Science (JSPS) KAKENHI Program (Grant No. 20K05453).

## ■ REFERENCES


(1) Mayer, K. M.; Hafner, J. H. Localized Surface Plasmon Resonance Sensors. *Chem. Rev.* **2011**, *111* (6), 3828−3857.

(2) Anker, J. N.; Hall, W. P.; Lyandres, O.; Shah, N. C.; Zhao, J.; Van Duyne, R. P. Biosensing with Plasmonic Nanosensors. *Nat. Mater.* **2008**, *7* (6), 442−453.

(3) Markel, V. A. Coupled-Dipole Approach to Scattering of Light from a One-Dimensional Periodic Dipole Structure. *J. Mod. Opt.* **1993**, *40* (11), 2281−2291.

(4) Zou, S.; Janel, N.; Schatz, G. C. Silver Nanoparticle Array Structures That Produce Remarkably Narrow Plasmon Lineshapes. *J. Chem. Phys.* **2004**, *120* (23), 10871−10875.

(5) Mulvaney, P. Surface Plasmon Spectroscopy of Nanosized Metal Particles. *Langmuir* **1996**, *12* (3), 788−800.

(6) Kravets, V. G.; Kabashin, A. V.; Barnes, W. L.; Grigorenko, A. N. Plasmonic Surface Lattice Resonances: A Review of Properties and Applications. *Chem. Rev.* **2018**, *118* (12), 5912−5951.

(7) Malynych, S.; Chumanov, G. Light-Induced Coherent Interactions between Silver Nanoparticles in Two-Dimensional Arrays. *J. Am. Chem. Soc.* **2003**, *125* (10), 2896−2898.

(8) Auguié, B.; Barnes, W. L. Collective Resonances in Gold Nanoparticle Arrays. *Phys. Rev. Lett.* **2008**, *101* (14), 143902.

(9) Hicks, E. M.; Zou, S.; Schatz, G. C.; Spears, K. G.; Van Duyne, R. P.; Gunnarsson, L.; Rindzevicius, T.; Kasemo, B.; Käll, M. Controlling Plasmon Line Shapes through Diffractive Coupling in Linear Arrays of Cylindrical Nanoparticles Fabricated by Electron Beam Lithography. *Nano Lett.* **2005**, *5* (6), 1065−1070.

(10) Henzie, J.; Lee, M. H.; Odom, T. W. Multiscale Patterning of Plasmonic Metamaterials. *Nat. Nanotechnol.* **2007**, *2* (9), 549−554.

(11) Kravets, V. G.; Schedin, F.; Grigorenko, A. N. Extremely Narrow Plasmon Resonances Based on Diffraction Coupling of Localized Plasmons in Arrays of Metallic Nanoparticles. *Phys. Rev. Lett.* **2008**, *101* (8), No. 087403.

(12) Zhou, W.; Odom, T. W. Tunable Subradiant Lattice Plasmons by Out-of-Plane Dipolar Interactions. *Nat. Nanotechnol.* **2011**, *6* (7), 423−427.

(13) Cherqui, C.; Bourgeois, M. R.; Wang, D.; Schatz, G. C. Plasmonic Surface Lattice Resonances: Theory and Computation. *Acc. Chem. Res.* **2019**, *52* (9), 2548−2558.

(14) Wang, W.; Ramezani, M.; Väkeväinen, A. I.; Törmä, P.; Rivas, J. G.; Odom, T. W. The Rich Photonic World of Plasmonic Nanoparticle Arrays. *Mater. Today* **2018**, *21* (3), 303−314.

(15) Goerlitzer, E. S. A.; Mohammadi, R.; Nechayev, S.; Volk, K.; Rey, M.; Banzer, P.; Karg, M.; Vogel, N. Chiral Surface Lattice Resonances. *Adv. Mater.* **2020**, *32*, 2001330.

(16) Wang, D.; Bourgeois, M. R.; Guan, J.; Fumani, A. K.; Schatz, G. C.; Odom, T. W. Lasing from Finite Plasmonic Nanoparticle Lattices. *ACS Photonics* **2020**, *7* (3), 630−636.

(17) Guan, J.; Sagar, L. K.; Li, R.; Wang, D.; Bappi, G.; Watkins, N. E.; Bourgeois, M. R.; Levina, L.; Fan, F.; Hoogland, S.; Voznyy, O.; Martins de Pina, J.; Schaller, R. D.; Schatz, G. C.; Sargent, E. H.; Odom, T. W. Engineering Directionality in Quantum Dot Shell Lasing Using Plasmonic Lattices. *Nano Lett.* **2020**, *20* (2), 1468−1474.

(18) Liu, Y.; Teitelboim, A.; Fernandez-Bravo, A.; Yao, K.; Altoe, M. V. P.; Aloni, S.; Zhang, C.; Cohen, B. E.; Schuck, P. J.; Chan, E. M. Controlled Assembly of Upconverting Nanoparticles for Low-

Threshold Microlasers and Their Imaging in Scattering Media. *ACS Nano* **2020**, *14* (2), 1508−1519.
(19) Vaskin, A.; Kolkowski, R.; Koenderink, A. F.; Staude, I. Light-Emitting Metasurfaces. *Nanophotonics* **2019**, *8* (7), 1151−1198.
(20) Hartland, G. V. Optical Studies of Dynamics in Noble Metal Nanostructures. *Chem. Rev.* **2011**, *111* (6), 3858−3887.
(21) Peckus, D.; Rong, H.; Stankevičius, L.; Juodėnas, M.; Tamulevičius, S.; Tamulevičius, T.; Henzie, J. Hot Electron Emission Can Lead to Damping of Optomechanical Modes in Core−Shell Ag@$TiO_2$ Nanocubes. *J. Phys. Chem. C* **2017**, *121* (43), 24159−24167.
(22) Link, S.; El-Sayed, M. A. Spectral Properties and Relaxation Dynamics of Surface Plasmon Electronic Oscillations in Gold and Silver Nanodots and Nanorods. *J. Phys. Chem. B* **1999**, *103* (40), 8410−8426.
(23) Voisin, C.; Del Fatti, N.; Christofilos, D.; Vallée, F. Ultrafast Electron Dynamics and Optical Nonlinearities in Metal Nanoparticles. *J. Phys. Chem. B* **2001**, *105* (12), 2264−2280.
(24) Besteiro, L. V.; Kong, X.-T.; Wang, Z.; Hartland, G.; Govorov, A. O. Understanding Hot-Electron Generation and Plasmon Relaxation in Metal Nanocrystals: Quantum and Classical Mechanisms. *ACS Photonics* **2017**, *4* (11), 2759−2781.
(25) Petrova, H.; Lin, C.-H. H.; De Liejer, S.; Hu, M.; McLellan, J. M.; Siekkinen, A. R.; Wiley, B. J.; Marquez, M.; Xia, Y.; Sader, J. E.; Hartland, G. V. Time-Resolved Spectroscopy of Silver Nanocubes: Observation and Assignment of Coherently Excited Vibrational Modes. *J. Chem. Phys.* **2007**, *126* (9), No. 094709.
(26) Hodak, J. H.; Martini, I.; Hartland, G. V. Spectroscopy and Dynamics of Nanometer-Sized Noble Metal Particles. *J. Phys. Chem. B* **1998**, *102* (36), 6958−6967.
(27) Ahmed, A.; Pelton, M.; Guest, J. R. Understanding How Acoustic Vibrations Modulate the Optical Response of Plasmonic Metal Nanoparticles. *ACS Nano* **2017**, *11* (9), 9360−9369.
(28) Staleva, H.; Hartland, G. V. Transient Absorption Studies of Single Silver Nanocubes. *J. Phys. Chem. C* **2008**, *112* (20), 7535−7539.
(29) Sun, Q.; Yu, H.; Ueno, K.; Kubo, A.; Matsuo, Y.; Misawa, H. Dissecting the Few-Femtosecond Dephasing Time of Dipole and Quadrupole Modes in Gold Nanoparticles Using Polarized Photoemission Electron Microscopy. *ACS Nano* **2016**, *10* (3), 3835−3842.
(30) Tretnak, V.; Hohenester, U.; Krenn, J. R.; Hohenau, A. The Role of Particle Size in the Dispersion Engineering of Plasmonic Arrays. *J. Phys. Chem. C* **2020**, *124* (3), 2104−2112.
(31) Robillard, J.-F.; Devos, A.; Roch-Jeune, I.; Mante, P. A. Collective Acoustic Modes in Various Two-Dimensional Crystals by Ultrafast Acoustics: Theory and Experiment. *Phys. Rev. B: Condens. Matter Mater. Phys.* **2008**, *78* (6), No. 064302.
(32) Eichenfield, M.; Chan, J.; Camacho, R. M.; Vahala, K. J.; Painter, O. Optomechanical Crystals. *Nature* **2009**, *462* (7269), 78−82.
(33) El-Jallal, S.; Mrabti, A.; Lévêque, G.; Akjouj, A.; Pennec, Y.; Djafari-Rouhani, B. Phonon Interaction with Coupled Photonic-Plasmonic Modes in a Phoxonic Cavity. *AIP Adv.* **2016**, *6* (12), 122001.
(34) Zhang, H.; Kinnear, C.; Mulvaney, P. Fabrication of Single-Nanocrystal Arrays. *Adv. Mater.* **2020**, *32* (18), 1904551.
(35) Lin, Q.-Y.; Li, Z.; Brown, K. A.; O'Brien, M. N.; Ross, M. B.; Zhou, Y.; Butun, S.; Chen, P.-C.; Schatz, G. C.; Dravid, V. P.; Aydin, K.; Mirkin, C. A. Strong Coupling between Plasmonic Gap Modes and Photonic Lattice Modes in DNA-Assembled Gold Nanocube Arrays. *Nano Lett.* **2015**, *15* (7), 4699−4703.
(36) Lin, Q.-Y.; Mason, J. A.; Li, Z.; Zhou, W.; O'Brien, M. N.; Brown, K. A.; Jones, M. R.; Butun, S.; Lee, B.; Dravid, V. P.; Aydin, K.; Mirkin, C. A. Building Superlattices from Individual Nanoparticles via Template-Confined DNA-Mediated Assembly. *Science (Washington, DC, U. S.)* **2018**, *359* (6376), 669−672.
(37) Ni, S.; Isa, L.; Wolf, H. Capillary Assembly as a Tool for the Heterogeneous Integration of Micro- and Nanoscale Objects. *Soft Matter* **2018**, *14* (16), 2978−2995.
(38) Tao, A.; Sinsermsuksakul, P.; Yang, P. Polyhedral Silver Nanocrystals with Distinct Scattering Signatures. *Angew. Chem., Int. Ed.* **2006**, *45* (28), 4597−4601.
(39) Henzie, J.; Grünwald, M.; Widmer-Cooper, A.; Geissler, P. L.; Yang, P. Self-Assembly of Uniform Polyhedral Silver Nanocrystals into Densest Packings and Exotic Superlattices. *Nat. Mater.* **2012**, *11* (2), 131−137.
(40) Henzie, J.; Andrews, S. C.; Ling, X. Y. Y.; Li, Z.; Yang, P. Oriented Assembly of Polyhedral Plasmonic Nanoparticle Clusters. *Proc. Natl. Acad. Sci. U. S. A.* **2013**, *110* (17), 6640−6645.
(41) Virganavičius, D.; Juodėnas, M.; Tamulevičius, T.; Schift, H.; Tamulevičius, S. Investigation of Transient Dynamics of Capillary Assisted Particle Assembly Yield. *Appl. Surf. Sci.* **2017**, *406* (11), 136−143.
(42) Juodėnas, M.; Tamulevičius, T.; Henzie, J.; Erts, D.; Tamulevičius, S. Surface Lattice Resonances in Self-Assembled Arrays of Monodisperse Ag Cuboctahedra. *ACS Nano* **2019**, *13* (8), 9038−9047.
(43) Fuchs, R. Theory of the Optical Properties of Ionic Crystal Cubes. *Phys. Rev. B* **1975**, *11* (4), 1732−1740.
(44) Zhang, S.; Bao, K.; Halas, N. J.; Xu, H.; Nordlander, P. Substrate-Induced Fano Resonances of a Plasmonic Nanocube: A Route to Increased-Sensitivity Localized Surface Plasmon Resonance Sensors Revealed. *Nano Lett.* **2011**, *11* (4), 1657−1663.
(45) Sherry, L. J.; Chang, S.-H.; Schatz, G. C.; Van Duyne, R. P.; Wiley, B. J.; Xia, Y. Localized Surface Plasmon Resonance Spectroscopy of Single Silver Nanocubes. *Nano Lett.* **2005**, *5* (10), 2034−2038.
(46) Huttunen, M. J.; Dolgaleva, K.; Törmä, P.; Boyd, R. W. Ultra-Strong Polarization Dependence of Surface Lattice Resonances with out-of-Plane Plasmon Oscillations. *Opt. Express* **2016**, *24* (25), 28279.
(47) Li, G. H. Y.; Li, G. Necessary Conditions for Out-of-Plane Lattice Plasmons in Nanoparticle Arrays. *J. Opt. Soc. Am. B* **2019**, *36* (4), 805.
(48) Zhou, W.; Hua, Y.; Huntington, M. D.; Odom, T. W. Delocalized Lattice Plasmon Resonances Show Dispersive Quality Factors. *J. Phys. Chem. Lett.* **2012**, *3* (10), 1381−1385.
(49) Yang, X.; Xiao, G.; Lu, Y.; Li, G. Narrow Plasmonic Surface Lattice Resonances with Preference to Asymmetric Dielectric Environment. *Opt. Express* **2019**, *27* (18), 25384.
(50) Hua, Y.; Fumani, A. K.; Odom, T. W. Tunable Lattice Plasmon Resonances in 1D Nanogratings. *ACS Photonics* **2019**, *6* (2), 322−326.
(51) McMahon, J. M.; Wang, Y.; Sherry, L. J.; Van Duyne, R. P.; Marks, L. D.; Gray, S. K.; Schatz, G. C. Correlating the Structure, Optical Spectra, and Electrodynamics of Single Silver Nanocubes. *J. Phys. Chem. C* **2009**, *113* (7), 2731−2735.
(52) Yi, C.; Dongare, P. D.; Su, M.-N.; Wang, W.; Chakraborty, D.; Wen, F.; Chang, W.-S.; Sader, J. E.; Nordlander, P.; Halas, N. J.; Link, S. Vibrational Coupling in Plasmonic Molecules. *Proc. Natl. Acad. Sci. U. S. A.* **2017**, *114* (44), 11621−11626.
(53) Guo, P.; Schaller, R. D.; Ocola, L. E.; Ketterson, J. B.; Chang, R. P. H. Gigahertz Acoustic Vibrations of Elastically Anisotropic Indium−Tin-Oxide Nanorod Arrays. *Nano Lett.* **2016**, *16* (9), 5639−5646.
(54) Huang, W.; Qian, W.; El-Sayed, M. A. Coherent Vibrational Oscillation in Gold Prismatic Monolayer Periodic Nanoparticle Arrays. *Nano Lett.* **2004**, *4* (9), 1741−1747.
(55) Wang, L.; Nishijima, Y.; Ueno, K.; Misawa, H.; Tamai, N. Near-IR Vibrational Dynamics of Periodic Gold Single and Pair Nanocuboids. *Appl. Phys. Lett.* **2009**, *95* (5), No. 053116.
(56) Devkota, T.; Chakraborty, D.; Yu, K.; Beane, G.; Sader, J. E.; Hartland, G. V. On the Measurement of Relaxation Times of Acoustic Vibrations in Metal Nanowires. *Phys. Chem. Chem. Phys.* **2018**, *20* (26), 17687−17693.
(57) Rycenga, M.; Langille, M. R.; Personick, M. L.; Ozel, T.; Mirkin, C. A. Chemically Isolating Hot Spots on Concave Nanocubes. *Nano Lett.* **2012**, *12* (12), 6218−6222.


https://dx.doi.org/10.1021/acsphotonics.0c01187
*ACS Photonics* 2020, 7, 3130−3140

(58) Pellarin, M.; Ramade, J.; Rye, J. M.; Bonnet, C.; Broyer, M.; Lebeault, M.-A.; Lermé, J.; Marguet, S.; Navarro, J. R. G.; Cottancin, E. Fano Transparency in Rounded Nanocube Dimers Induced by Gap Plasmon Coupling. *ACS Nano* **2016**, *10* (12), 11266−11279.
(59) Wang, W.; Watkins, N.; Yang, A.; Schaller, R. D.; Schatz, G. C.; Odom, T. W. Ultrafast Dynamics of Lattice Plasmon Lasers. *J. Phys. Chem. Lett.* **2019**, *10* (12), 3301−3306.
(60) Tamulevičius, T.; Gražulevičiutė, I.; Urbonas, D.; Gabalis, M.; Petruškevičius, R.; Tamulevičius, S. Numerical and Experimental Analysis of Optical Response of Sub-Wavelength Period Structure in Carbonaceous Film for Refractive Index Sensing. *Opt. Express* **2014**, *22* (22), 27462.
(61) Johnson, P. B.; Christy, R. W. Optical Constants of the Noble Metals. *Phys. Rev. B* **1972**, *6* (12), 4370−4379.


https://dx.doi.org/10.1021/acsphotonics.0c01187
*ACS Photonics* 2020, 7, 3130−3140